The Effects of Layers in Dry Snow on Its Passive Microwave Emissions Using Dense Media Radiative Transfer Theory Based on the Quasicrystalline Approximation (QCA/DMRT)

Ding Liang, *Student Member, IEEE*, Xiaolan Xu, Leung Tsang, *Fellow, IEEE*, Konstantinos M. Andreadis, and Edward G. Josberger

***Abstract*—A model for the microwave emissions of multilayer dry snowpacks, based on dense media radiative transfer (DMRT) theory with the quasicrystalline approximation (QCA), provides more accurate results when compared to emissions determined by a homogeneous snowpack and other scattering models. The DMRT model accounts for adhesive aggregate effects, which leads to dense media Mie scattering by using a sticky particle model. With the multilayer model, we examined both the frequency and polarization dependence of brightness temperatures (Tb's) from representative snowpacks and compared them to results from a single-layer model and found that the multilayer model predicts higher polarization differences, twice as much, and weaker frequency dependence. We also studied the temporal evolution of Tb from multilayer snowpacks. The difference between Tb's at 18.7 and 36.5 GHz can be 5 K lower than the single-layer model prediction in this paper. By using the snowpack observations from the Cold Land Processes Field Experiment as input for both multi- and single-layer models, it shows that the multilayer Tb's are in better agreement with the data than the single-layer model. With one set of physical parameters, the multilayer QCA/DMRT model matched all four channels of Tb observations simultaneously, whereas the single-layer model could only reproduce vertically polarized Tb's. Also, the polarization difference and frequency dependence were accurately matched by the multilayer model using the same set of physical parameters. Hence, algorithms for the retrieval of snowpack depth or water equivalent should be based on multilayer scattering models to achieve greater accuracy.**

***Index Terms*—Dense media, dense media radiative transfer (DMRT) theory, layered media, microwave remote sensing, snow.**

I. Introduction

MICROWAVE remote sensing signatures of snowpacks result from the interaction of the electromagnetic radiation and the snow properties: depth, density, grain size, wetness, and stickiness. A scattering model that can simulate the scattering from a complex structure of snowpack is needed to develop algorithms for the retrieval of snow parameters, particularly snow water equivalent from satellite observations. An earlier version of dense media radiative transfer (DMRT) theory was derived for grain sizes smaller than the wavelength and nonsticky particles [1]. The resulting phase matrix is the Rayleigh phase matrix, and the scattering coefficient has a fourth-power frequency dependence. In the Helsinki University of Technology (HUT) snow emission model [2], the frequency dependence of extinction coefficient is empirically determined. HUT assumes that scattered energy is mostly concentrated in the forward direction, whereas scattering in other directions is ignored. This corresponds to a Dirac delta function in the phase matrix. HUT simulations agree well with vertically polarized brightness temperature measurements; however, it poorly reproduces horizontally polarized brightness temperatures. The microwave emission model of layered snowpacks (MEMLS) [3] is based on strong fluctuation theory [4]. The frequency dependence of scattering coefficient is empirically determined. MEMLS assumes equal forward and backward scattering. The extension model of the MEMLS to coarse-grained snow [5] uses the Rayleigh phase matrix, so scattering coefficient has a fourth-power dependence on frequency. The QCA/DMRT model of sticky particles is a physical model [6], which includes the collective scattering among the particles. The pair distribution functions of the Percus–Yevick approximations for sticky particles are used to simulate the adhesion of ice grains and the formation of aggregates. Thus, higher order multipoles beyond the electric dipole are used to account for the aggregate effects resulting in dense Mie scattering. The QCA/DMRT model gives the following different results when compared to classical independent scattering theory: 1) The extinction saturates at high fractional volume; 2) the scattering coefficient has a frequency dependence that is weaker than the fourth power; 3) the mean cosine of the phase matrix is not zero; and 4) the phase matrix shows more forward scattering and has a larger mean cosine than the classical Mie scattering theory of the same grain size. The same set of DMRT equations is used for both active and passive remote sensing in the QCA/DMRT model. The only difference is the excitation in the DMRT equations: for active remote sensing, the excitation is from radar, whereas for passive remote sensing, the excitation is from

Manuscript received January 31, 2008. Current version published October 30, 2008. This work was supported in part by the U.S. National Aeronautics and Space Administration.

D. Liang, X. Xu, and L. Tsang are with the Department of Electrical Engineering, University of Washington, Seattle, WA 98195 USA (e-mail: dingl@U.washington.edu).

K. M. Andreadis is with the Department of Civil and Environmental Engineering, University of Washington, Seattle, WA 98195 USA.

E. G. Josberger is with the U.S. Geological Survey, Washington Water Science Center, Tacoma, WA 98402 USA.

Color versions of one or more of the figures in this paper are available online at http://ieeexplore.ieee.org.

Digital Object Identifier 10.1109/TGRS.2008.922143

ground emission. The HUT model has not been applied to active remote sensing. Recently, the original QCA/DMRT sticky Mie model [6] was simplified in 1–2 frame, giving relatively simple mathematical expressions of the phase matrix in the 1–2 frame [7]. Phase matrices in the 1–2 frame were illustrated and compared with other models [7].

For a single-layer snowpack, Chang *et al.* [8] assumed that the difference between 18.7- and 36.5-GHz brightness temperatures is proportional to snow depth or water equivalent. Chang's algorithm works for thin to moderate snow depth, whereas it does not work for thick snow because the 37-GHz Tb saturates at snow depths of between 50 and 100 cm, depending on the grain size and volume fraction components. Hence, Chang's algorithm fails once the snow depth reaches approximately 50–100 cm. Andreadis *et al.* [9] evaluated the coupled variable infiltration capacity snow hydrology model and single-layer microwave emission model using multiscale brightness temperature measurements from the Cold Land Processes Field Experiment (CLPX). Various single-layer snow microwave emission models have some success [10]; however, they quite often fail to reproduce important observed snowpack microwave emission features. Andreadis *et al.* [9] found that the polarization difference estimated by the single-layer QCA/DMRT model is about half of the ground observation. A natural snowpack has a layered structure with different snow densities and grain sizes at different layers because of the episodic accumulation and snow metamorphism [11], which results in very different microwave signatures [12] when compared to a single layer of comparable thickness. Sturm and Holmgren [13] classified the seasonal snow covers into six classes, with each class being defined by a unique ensemble of texture and stratigraphic characteristics. Rosenfeld and Grody [14] studied the anomalous microwave spectra of snow cover observed from the Special Sensor Microwave Imager (SSM/I) and found two anomalies in the microwave spectra. One anomaly is that Tb reaches a minimum around the middle of winter and then increases despite the fact that snow depth remains constant or even continues to thicken. Another is the inversion of brightness temperature spectra, where Tb of higher frequency is larger than those of lower frequency, which is thought to be caused when a dense layer of surface crust forms on top of old coarse-grained snow. Microwave emission models based on layered snow structure have been previously developed, but they do not adequately reproduce the observed behavior. Tedesco *et al.* [15] used a multilayer DMRT (QCA-CP) model to simulate emission from both wet and dry snows for a two-layer model, where the first layer was dry snow and the second layer was wet snow. Since the wet snow can be considered as a blackbody, the model of Tedesco *et al.* does not include the effects of multiple layers of dry snow on microwave emission, scattering, and reflection.

In this paper, we used a multilayered DMRT/QCA with a sticky particle Mie scattering model to simulate the brightness temperature emissions from a layered snowpack. The number of layers is variable. We solve for the radiation intensities at 16 Gaussian quadrature angles of zenith angle for every azimuth angle in every layer and use spline interpolation to interpolate the intensities at other angles, with the same physical angles in each layer. Reflection and refraction layer interfaces are included, and we use a cubic spline to interpolate the refracted radiation at the quadrature angles at the snow–snow interface. The layered structure is essential to analyze the microwave emissions from snow because of the following reasons: 1) Lower frequencies have greater penetration depth and have an integrated effect over the entire snowpack. On the other hand, higher frequencies are sensitive to snow properties near the surface. Thus, the frequency dependence of microwave emission from multilayer snow is different from those of single layer. 2) In layered snow, microwave radiation is reflected and refracted at the interfaces between snow layers. Because reflectivity for horizontally polarized emissions is greater than for the vertical case, the horizontally polarized brightness temperatures are lower for a layered snowpack.

Next, in Section II, we describe the DMRT equations for the multilayer snow model. The multiple scattering equations are exactly solved using 16 quadrature angles. The results include all orders of multiple scattering within the DMRT theory. Then, in Section III, we describe the effect of layering within a snowpack on the numerical calculated brightness temperatures. Finally, in Section IV, we compare the brightness temperature predictions from the multilayer scattering model with Ground-Based Passive Microwave Radiometer (GBMR-7) measurements at the Local Scale Observation Site (LSOS) of CLPX in Colorado, USA. We also compare the emissivities from the multilayer model with measurements at Davos, Switzerland, by Wiesmann *et al.* [16]. In both cases, the results are in better agreement than that found using a single-layer scattering model.

II. DMRT Equations for Multilayer Snow Model and Multiple Scattering Solutions

The multilayer snow structure is shown in Fig. 1(a). There are N layers of snow with the iith layer of snow from $z = -d_{ii-1}$ to $z = -d_{ii}$, where $ii = 1, 2, \ldots, N$. The air–snow boundary is at $z = d_0 = 0$, and the snow–ground boundary is at $z = d_N = d$. In every layer, the microwave emission follows the DMRT equations. We consider full multiple scattering effects with 16 Gaussian quadrature angles. The same 16 angles are used in every layer. Because the angles of different layers are related by Snell's law, we use a cubic spline interpolation to interpolate from the angles of Snell's law to the quadrature angles. Fig. 1(b) shows the transmission of microwave at the 16 quadrature angles from layer $ii+1$ to layer ii when $\varepsilon_{ii+1} < \varepsilon_{ii}$; θ_c is the critical angle in layer ii. Because the wave paths deviate from the quadrature angles in layer ii, we interpolate the intensities at quadrature angles in layer ii from the refractive intensities. The DMRT equations for passive remote sensing can be derived from the DMRT equations for active remote sensing [7, eqs. (17a)–(18b)], as the equations are simplified because of azimuthal symmetry for the passive remote sensing case. The specific intensities are not dependent on the angle ϕ

$$\cos\theta \frac{\mathrm{d}\overline{I}_{ii}(\theta, z)}{\mathrm{d}z} = -\kappa_{eii} \cdot \overline{I}_{ii}(\theta, z) + \overline{S}_{ii}(\theta, z) + \kappa_a \overline{T}^{ii} \tag{1a}$$

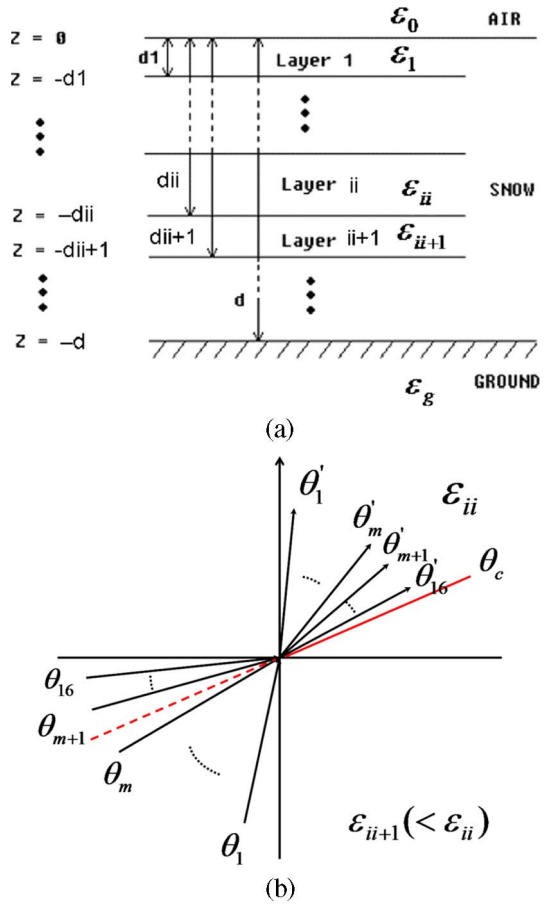

Fig. 1. (a) Configuration of a layered medium. (b) Wave refraction from layer $ii+1$ to layer ii.

$$-\cos\theta\frac{\mathrm{d}\overline{I}_{ii}(\pi-\theta,z)}{\mathrm{d}z} = -\kappa_{eii}\cdot\overline{I}_{ii}(\pi-\theta,z)+\overline{W}_{ii}(\theta,z)+\kappa_a\overline{T}^{ii} \tag{1b}$$

$$\overline{S}_{ii}(\theta,z) = \int_0^{\pi/2}\mathrm{d}\theta'\sin\theta'\int_0^{2\pi}\mathrm{d}\phi\overline{\overline{P}}_{ii}(\theta,\phi;\theta',\phi'=0)\overline{I}_{ii}(\theta',z) + \int_0^{\pi/2}\mathrm{d}\theta'\sin\theta'\int_0^{2\pi}\mathrm{d}\phi\overline{\overline{P}}_{ii}(\theta,\phi;\pi-\theta',\phi'=0) \times\overline{I}_{ii}(\pi-\theta',z) \tag{2a}$$

$$\overline{W}_{ii}(\theta,z) = \int_0^{\pi/2}\mathrm{d}\theta'\sin\theta'\int_0^{2\pi}\mathrm{d}\phi\overline{\overline{P}}_{ii}(\pi-\theta,\phi;\theta',\phi'=0)\overline{I}_{ii}(\theta',z) + \int_0^{\pi/2}\mathrm{d}\theta'\sin\theta'\int_0^{2\pi}\mathrm{d}\phi\overline{\overline{P}}_{ii}(\pi-\theta,\phi;\pi-\theta',\phi'=0) \times\overline{I}_{ii}(\pi-\theta',z) \tag{2b}$$

where $\overline{I}_{ii}(\theta,z)$ is the specific intensity of both vertical and horizontal polarizations at any Gaussian quadrature angle θ in the iith layer, and $\overline{\overline{P}}_{ii}$ is the phase matrix in the iith layer. The simplified form of $\overline{\overline{P}}$ in 1–2 frame is in [7, eq. (16)]. We use the same equation here to calculate $\overline{\overline{P}}_{ii}$. κ_{eii} is the extinction coefficient in the iith layer, which can be calculated by [7, eqs. (4) and (12)]. Details of solving the differential equations for each layer can be found in [4].

The parameters P_l and P_{-l} in [4, eqs. (30) and (31)] can be solved by matching the boundary conditions, which are

$$\text{At}\quad z=0,$$
$$\overline{I}_1(\pi-\theta,z=0)=\overline{\overline{R}}_{10}(\theta)\overline{I}_1(\theta,z=0) \tag{3a}$$
$$\text{At}\quad z=-d_j,\qquad j=1,2,\ldots,N1,$$
$$\overline{I}_j(\theta,z=-d_j)=\overline{\overline{R}}_{j,j+1}(\theta)\overline{I}_j(\pi-\theta,z=-d_j) + \overline{\overline{S}}_{j+1,j}(\theta)\overline{\overline{T}}_{j+1,j}(\theta) \times\overline{I}_{j+1}(\theta,z=-d_j) \tag{3b}$$
$$\overline{I}_{j+1}(\pi-\theta,z=-d_j)=\overline{\overline{R}}_{j+1,j}(\theta)\overline{I}_{j+1}(\theta,z=-d_j) + \overline{\overline{S}}_{j,j+1}(\theta)\overline{\overline{T}}_{j,j+1}(\theta) \times\overline{I}_j(\pi-\theta,z=-d_j) \tag{3c}$$
$$\text{At}\quad z=-d,$$
$$\overline{I}_n(\theta,z=-d)=\overline{\overline{R}}_{ng}(\theta)\overline{I}_n(\pi-\theta,z=-d) + \overline{\overline{T}}_{gn}(\theta)T_g. \tag{3d}$$

$\overline{\overline{R}}_{10}(\theta)$, $\overline{\overline{R}}_{ng}(\theta)$, $\overline{\overline{R}}_{j,j+1}(\theta)$, and $\overline{\overline{R}}_{j+1,j}(\theta)$ are the reflectivity matrices at snow–air, snow–ground, and snow–snow boundaries. $\overline{\overline{T}}_{j+1,j}(\theta)$, $\overline{\overline{T}}_{j,j+1}(\theta)$, and $\overline{\overline{T}}_{gn}(\theta)$ are the transmissivity matrices from snow to snow and from ground to snow. We account for the roughness only at the snow–ground interface by the following. We use the Q/H model [17], with $\overline{R}_{ng\_H}=((1-Q)\cdot\overline{R}_H+Q\cdot\overline{R}_V)\cdot e^{-H\cdot\overline{\mu}^2}$ and $\overline{R}_{ng\_V}=((1-Q)\cdot\overline{R}_V+Q\cdot\overline{R}_H)\cdot e^{-H\cdot\overline{\mu}^2}$, where $\overline{R}_{ng\_H}$ and $\overline{R}_{ng\_V}$ are the reflectivities of the horizontal and vertical polarizations at rough snow–ground interface, respectively. $\overline{R}_H$ and $\overline{R}_V$ are the corresponding reflectivities for the smooth interface. $\overline{\mu}$ is a vector of cosine values for the Gaussian quadrature angles. $\overline{\overline{S}}_{j,j+1}(\theta)$ and $\overline{\overline{S}}_{j+1,j}(\theta)$ are the interpolation matrices.

We use a cubic spline with a "not a knot" end condition [18] to interpolate from the angles of Snell's law to the quadrature angles. We have $n(n=16)$ wave paths with angles $\theta_1,\ldots,\theta_n$ that refract from layer with ε_{ii+1} to layer with ε_{ii}, $\varepsilon_{ii+1}<\varepsilon_{ii}$, as shown in Fig. 1(b). The n refraction angles $\theta'_1,\ldots,\theta'_n$ are smaller than the critical angle θ_c. If $\theta_m<\theta_c\le\theta_{m+1}$, where $m<n$, then the refracted intensities at angles from θ_{m+1} to θ_n are zeros. Then, we only need to interpolate the intensities from θ_1 to θ_m from the intensities from θ'_1 to θ'_n.

To solve these equations, we proceed as follows. Let $X_1=\cos\theta'_1,\ldots,X_n=\cos\theta'_n$. Then, sort the vector of X, and get $[x_1,\ldots,x_n]=[X_n,\ldots,X_1]$. The intensities at these angles are $g(x_1),\ldots,g(x_n)$, respectively. The piecewise cubic interpolant f to g is that, on interval $[x_i,x_{i+1}]$, we have f agree

with some polynomial P_i of order four, with $f(x) = P_i(x)$ for $x_i \le x \le x_{i+1}$, where $i = 1, \ldots, n-1$.

The ith polynomial piece P_i satisfies $P_i(x_i) = g(x_i)$, $P_i(x_{i+1}) = g(x_{i+1})$, $P_i'(x_i) = s_i$, and $P_i'(x_{i+1}) = s_{i+1}$, where $i = 1, \ldots, n-1$.

We use the Newton form for the ith polynomial piece P_i

$$\begin{aligned} P_i(x) &= P_i(x_i) + (x-x_i)P_i'(x_i) + (x-x_i)^2 P_i''(x_i)/2 \\ &\quad + (x-x_i)^3 P_i'''(x_i)/6 \\ &= \left[1 - 3(x-x_i)^2/(x_{i+1}-x_i)^2 \right. \\ &\quad \left. + 2(x-x_i)^3/(x_{i+1}-x_i)^3\right] \cdot g(x_i) \\ &\quad + \left[3(x-x_i)^2/(x_{i+1}-x_i)^2 \right. \\ &\quad \left. - 2(x-x_i)^3/(x_{i+1}-x_i)^3\right] \cdot g(x_{i+1}) \\ &\quad + \left[(x-x_i) - 2(x-x_i)^2/(x_{i+1}-x_i) \right. \\ &\quad \left. + (x-x_i)^3/(x_{i+1}-x_i)^2\right] \cdot s_i \\ &\quad + \left[(x-x_i)^2(x-x_{i+1})/(x_{i+1}-x_i)^2\right] \cdot s_{i+1}. \end{aligned} \tag{4}$$

Define $\overline{s} = [s_1, \ldots, s_n]'$, and $\overline{g} = [g(x_1), \ldots, g(x_n)]'$. $\overline{\overline{c}}$ and $\overline{\overline{t}}$ are $n \times n$ matrices,

$$\overline{\overline{c}}(1,1) = x_3 - x_2 \tag{5a}$$

$$\overline{\overline{c}}(1,2) = x_3 - x_1 \tag{5b}$$

$$\overline{\overline{c}}(k,k-1) = x_{k+1} - x_k \tag{5c}$$

$$\overline{\overline{c}}(k,k) = 2(x_{k+1} - x_{k-1}) \tag{5d}$$

$$\overline{\overline{c}}(k,k+1) = x_k - x_{k-1}, k = 2, \ldots, n-1 \tag{5e}$$

$$\overline{\overline{c}}(n,n-1) = x_n - x_{n-2} \tag{5f}$$

$$\overline{\overline{c}}(n,n) = x_{n-1} - x_{n-2} \tag{5g}$$

$$\begin{aligned} \overline{\overline{t}}(1,1) &= -(x_3 - x_2)\cdot(2x_3 + x_2 - 3x_1) \\ &\quad /(x_2 - x_1)/(x_3 - x_1) \end{aligned} \tag{6a}$$

$$\begin{aligned} \overline{\overline{t}}(1,2) &= (x_3 - x_2)\cdot(2x_3 + x_2 - 3x_1) \\ &\quad /(x_2 - x_1)/(x_3 - x_1) - (x_2 - x_1)^2 \\ &\quad /(x_3 - x_2)/(x_3 - x_1) \end{aligned} \tag{6b}$$

$$\overline{\overline{t}}(1,3) = (x_2 - x_1)^2/(x_3 - x_2)/(x_3 - x_1) \tag{6c}$$

$$\overline{\overline{t}}(k,k-1) = -3(x_{k+1} - x_k)/(x_k - x_{k-1}) \tag{6d}$$

$$\begin{aligned} \overline{\overline{t}}(k,k) &= 3(x_{k+1} - x_k)/(x_k - x_{k-1}) \\ &\quad - 3(x_k - x_{k-1})/(x_{k+1} - x_k) \end{aligned} \tag{6e}$$

$$\overline{\overline{t}}(k,k+1) = 3(x_k - x_{k-1})/(x_{k+1} - x_k) \tag{6f}$$

$$\begin{aligned} \overline{\overline{t}}(n,n-2) &= -(x_n - x_{n-1})^2/(x_{n-1} - x_{n-2}) \\ &\quad /(x_n - x_{n-2}) \end{aligned} \tag{6g}$$

$$\begin{aligned} \overline{\overline{t}}(n,n-1) &= -(x_{n-1} - x_{n-2})\cdot(3x_n - x_{n-1} - 2x_{n-2}) \\ &\quad /(x_n - x_{n-1})/(x_n - x_{n-2}) + (x_n - x_{n-1})^2 \\ &\quad /(x_{n-1} - x_{n-2})/(x_n - x_{n-2}) \end{aligned} \tag{6h}$$

$$\begin{aligned} \overline{\overline{t}}(n,n) &= (x_{n-1} - x_{n-2})\cdot(3x_n - x_{n-1} - 2x_{n-2}) \\ &\quad /(x_n - x_{n-1})/(x_n - x_{n-2}) \end{aligned} \tag{6i}$$

$$\overline{\overline{d}} = \overline{\overline{c}}^{-1} \cdot \overline{\overline{t}}. \tag{7}$$

Then, we have $\overline{s} = \overline{\overline{d}} \cdot \overline{g}$. The ith polynomial piece can be written as $P_i(x) = \overline{p}_i(x) \cdot \overline{g}$, in which case

$$\begin{aligned} \overline{p}_i(x) &= \left[1 - 3(x-x_i)^2/(x_{i+1}-x_i)^2 \right. \\ &\quad \left. + 2(x-x_i)^3/(x_{i+1}-x_i)^3\right] \\ &\quad \cdot [0, \ldots, 0, \underset{i}{1}, 0, \ldots, 0] \\ &\quad + \left[3(x-x_i)^2/(x_{i+1}-x_i)^2 \right. \\ &\quad \left. - 2(x-x_i)^3/(x_{i+1}-x_i)^3\right] \\ &\quad \cdot [0, \ldots, 0, \underset{i+1}{1}, 0, \ldots, 0] \\ &\quad + \left[(x-x_i) - 2(x-x_i)^2/(x_{i+1}-x_i) \right. \\ &\quad \left. + (x-x_i)^3/(x_{i+1}-x_i)^2\right] \cdot \overline{\overline{d}}(i,:) \\ &\quad + \left[(x-x_i)^2(x-x_{i+1})/(x_{i+1}-x_i)^2\right] \cdot \overline{\overline{d}}(i+1,:). \end{aligned} \tag{8}$$

Also, let $x_1' = \cos\theta_1, \ldots, x_n' = \cos\theta_n$. The intensities at these angles are $f(x_1'), \ldots, f(x_n')$. We know that $f(x_{m+1}'), \ldots, f(x_n')$ are zeros. $f(x_1'), \ldots, f(x_m')$ can be calculated from $\overline{g}$ by

$$[f(x_1'), f(x_2'), \ldots, f(x_m')]' = \overline{\overline{p}} \cdot \overline{g}. \tag{9}$$

$\overline{\overline{p}}$ is an $m \times n$ matrix. The $jj(1 \le jj \le m)$th line of $\overline{\overline{p}}$ is filled by the following procedure.

If $x_{jj}' < x_1$, then $f(x_{jj}') = P_1(x_{jj}')$, $\overline{\overline{p}}(jj,:) = \overline{p}_1(x_{jj}')$. If $x_i \le x_{jj}' < x_{i+1}$, then $f(x_{jj}') = P_i(x_{jj}')$, and $\overline{\overline{p}}(jj,:) = \overline{p}_i(x_{jj}')$. Furthermore, if $x_n \le x_{jj}'$, then $f(x_{jj}') = P_{n-1}(x_{jj}')$, and $\overline{\overline{p}}(jj,:) = \overline{p}_{n-1}(x_{jj}')$.

We define the $\overline{\overline{s}}$ matrix by $\overline{\overline{s}}(:,l) = \overline{\overline{p}}(:, n-l+1)$, where $l = 1, \ldots, n$. Finally, the $n \times n$ interpolation matrix is $\overline{\overline{S}}_{j,j+1}(\theta') = [\overline{\overline{s}}; 0]$.

If $\varepsilon_{ii+1} > \varepsilon_{ii}$, the critical angle in region $ii+1$ is θ_c'. If $\theta_m < \theta_c' \le \theta_{m+1}$, where $m < n$, then m out of the n paths would be refracted. Refraction angles are $\theta_1', \ldots, \theta_m'$, similar to the case of $\varepsilon_{ii+1} < \varepsilon_{ii}$. We could interpolate the intensities in media 2 at angles from θ_1 to θ_n from the intensities at angles from θ_1' to θ_m'. In this case, $\overline{\overline{s}}$ is an $n \times m$ matrix, and $\overline{\overline{S}}_{j,j+1}(\theta') = [\overline{\overline{s}}, 0]$. The intensity in the air region, which gives the brightness temperature, is the intensity that is transmitted for the first layer. $T_b(\theta) = \overline{\overline{T}}_{10}(\theta) \cdot \overline{I}_1(\theta, z=0)$, where $\overline{\overline{T}}_{10}(\theta)$ is the transmissivity matrix from the snow region to the air region.

III. Results and Discussion

For all of the simulations that we carried out, we kept certain parameters and conditions constant while varying the

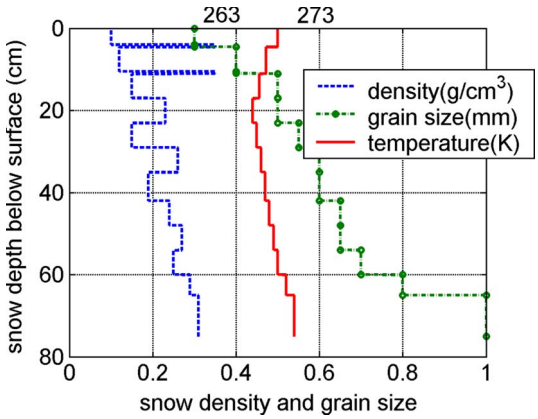

Fig. 2. Snow profile of grain size, density, and temperature. The numbers in the bottom of the profile are the values of snow density and grain size, whereas the numbers in the top are the snow temperatures.

snow depth and number and thickness of layers. We kept the stickiness parameter "τ" equal to 0.1 for every layer. Stickiness parameter is a concept that is borrowed from molecular physics. It is used to describe the potential energy of adhesiveness between particles [19]. Particle positions are determined by interparticle potential energy. Given the potential energy, one solves the Percus–Yevick equation to calculate the pair distribution function, which is proportional to the joint probability density functions of two particles. In QCA/DMRT, we consider the collective scattering between particles, which depends on the relative positions of the particles that are described by the pair distribution function. We chose $\tau = 0.1$ because it yields 2.8 for the frequency dependence of the extinction coefficient, which corresponds to the experimental values [20]. We use $\tau = 0.1$ for every layer because there are no studies that indicate how it varies; however, other values can be used if warranted by new studies.

We kept the ground temperature at 271 K, and the observation angle was 55°, the same as with the AMSR satellite, unless stated otherwise. The ice grains in snow have relative permittivities of $3.2 + 0.01i$ for 36.5 GHz and $3.2 + 0.001i$ for 18.7 GHz. The ground dielectric constant is $3.5 + 0.01i$. When computing the fractional volume from snow density, we used an ice density of 0.92 g/cm^3. We simulated the brightness temperatures for the snow profile shown in Fig. 2. The snow profile feature is from CLPX ground measurements at LSOS [21]. The snow densities fluctuate but generally increase as the snow depth increases. The snow grain sizes increase as the snow depth increases. The larger density fluctuations near the snow surface are due to the presence of a thin crust. The snow temperature decreases at first and then increases as the snow depth increases. We compared the multilayer snow model simulation results with that of a homogeneous single-layer snow model. For the single layer, the snow parameters are from the geometrically averaged values of the snow profile in Fig. 2. The results of the single-layer model with smooth and rough snow–ground interfaces, along with the results of the multilayer model with smooth and rough snow–ground interfaces, are shown in Table I. The roughness parameters are $Q = 0.35$ and $H = 1.2$.

TABLE I
BRIGHTNESS TEMPERATURE SIMULATION FOR FIG. 2

channel	Single-layer Smooth(K)	Multi-layer smooth(K)	Single-layer Rough(K)	Multi-layer Rough(K)
18.7v	241.3	241.2	240.5	240.9
18.7h	215.7	209	226.6	216.8
36.5v	207.4	208.9	207.6	209
36.5h	192.8	188.5	193.1	188.7
18.7v-18.7h	25.6	32.2	15.7	24.1
36.5v-36.5h	14.6	20.4	14.5	20.3
18.7v-36.5v	33.9	32.3	32.9	31.9
18.7h-36.5h	22.9	20.5	33.5	28.1

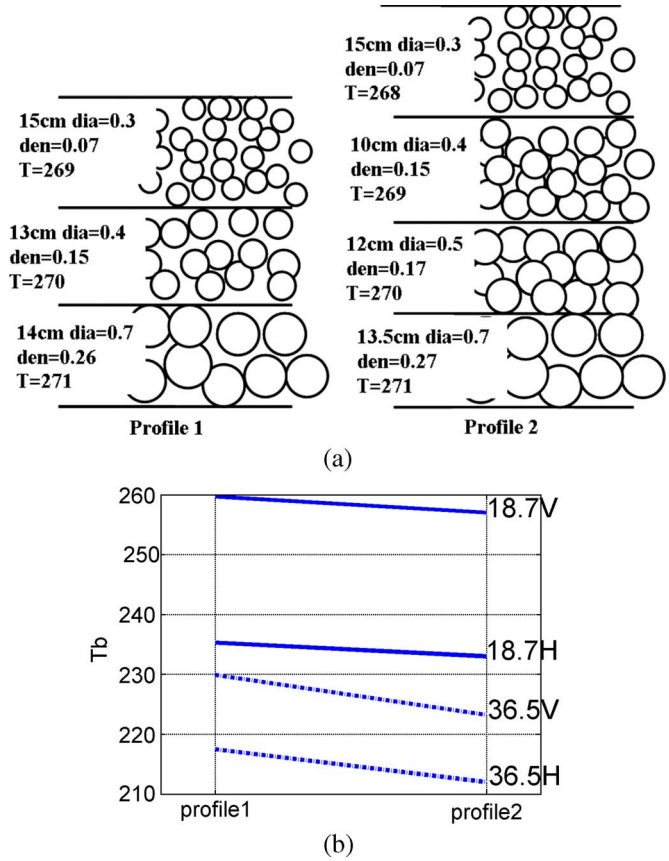

Fig. 3. Dependence of Tb on new snow layers on thick snow. (a) Snow profiles. Dia = diameter, den = density, and T = temperature. (b) Tb's for different profiles.

For smooth conditions, the model simulations show the following three features between the single- and multiple-layer model predictions.

1) The 36.5v Tb increases, whereas the 18.7v Tb does not have an obvious change. This is because the grain sizes in the penetration depth of 36.5 GHz in the multilayer model are smaller than those in the single-layer model. The 18.7v Tb depends on the average grain size.
2) Both 18.7h and 36.6h brightness temperatures decrease in the layered case. This is due to more reflections in a multilayer snow model.
3) The 18.7h Tb decreases from 215.7 K to 209 K, and the 36.5h Tb decreases from 192.8 K to 188.5 K. The 18.7h Tb decreases more than 36.5h Tb because the penetration

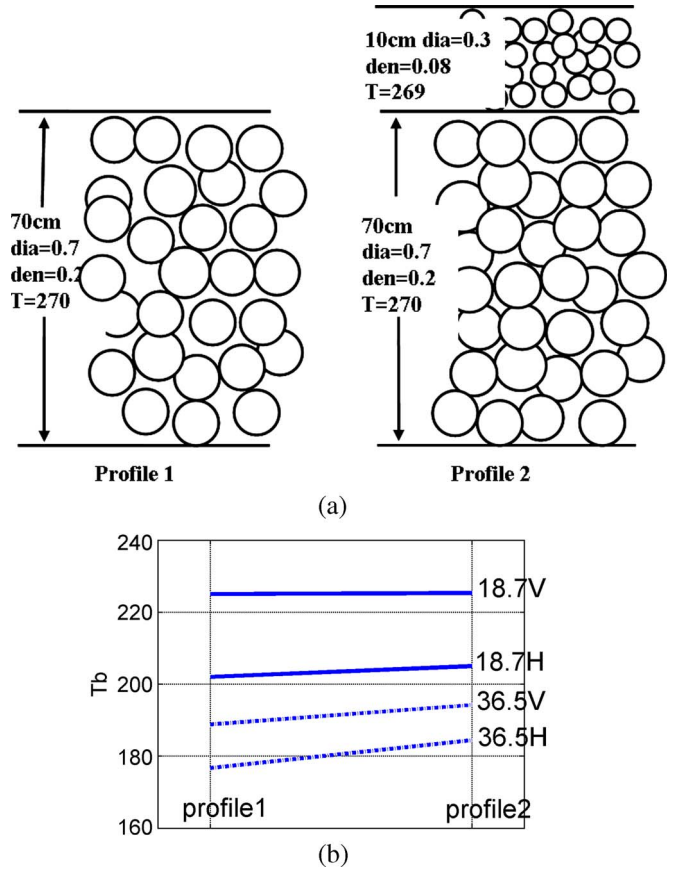

Fig. 4. Dependence of Tb on new snow layers on thick snow. (a) Snow profiles. (b) Tb's for different profiles.

depth of 18.7 GHz is greater than that of 36.5 GHz; hence, there are more reflections to influence the 18.7h Tb than the 36.5h Tb.

Therefore, for the multilayer case, 1) and 2) result in greater polarization differences, whereas 1) and 3) result in lower frequency differences. The polarization difference for 18.7 GHz is about 10 K higher than for 36.5 GHz in the smooth model. This is because 18.7 GHz could penetrate the snow–ground interface, which increases polarization effects at 18.7 GHz. For rough conditions at the snow–ground interface, we still find the aforementioned three features, so the rough multilayer model still predicts higher polarization differences and a lower frequency dependence than does the rough single-layer model.

A comparison of the smooth multilayer model with the rough one shows the following. There is no obvious impact on the 18.7v Tb, whereas the 18.7h Tb is obviously higher in the rough model than in the smooth one. This is because the rough ground reflection is smaller than the smooth one. These also lead to smaller polarization differences at 18.7 GHz in the rough case than in the smooth case. Because rough ground is not a major contribution to polarization difference, the snow density fluctuation near the air–snow interface dominates. The difference in the penetration depth of both 18.7 and 36.5 GHz leads to comparable polarization difference for both frequencies.

We also simulated the temporal Tb emission for three hypothetical, but realistic, snowpacks to examine the impact of layers on the microwave emissions. Fig. 3(a) shows two snow

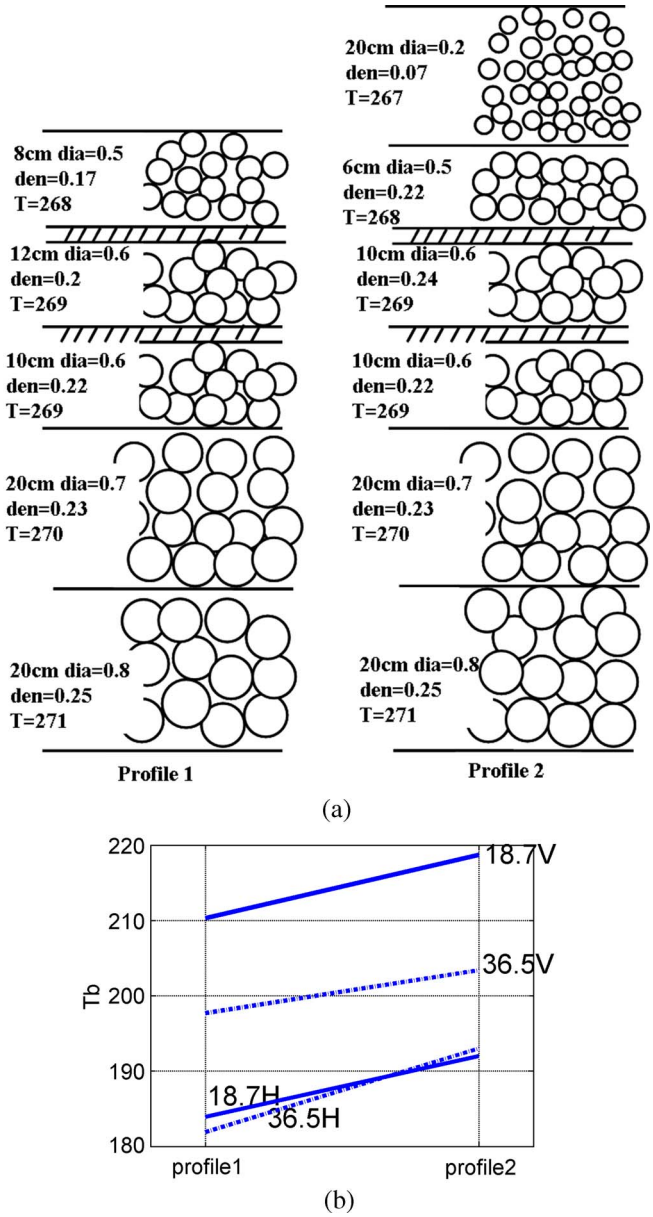

Fig. 5. Dependence of Tb on new snow layers on thick snow. The dark layer is a crust. (a) Snow profiles. (b) Tb's for different profiles.

profiles of two days with new snow accumulation every day, and Fig. 3(b) shows Tb simulation of these two profiles. We can see that Tb decreases as new snow accumulates because, as snow depth increases, the attenuation effects on the ground emission increases. The attenuation effects are greater for higher frequencies; therefore, the 36.5-GHz Tb decreases faster than that at 18.7 GHz. This leads to increasing differences between the two frequencies as the snow accumulates. Thus, the multilayer model exhibits the expected brightness temperature dependence on accumulation of new snow.

To simulate the effects of a new snow fall on a thick snowpack, we add 10 cm of fine-grained snow to a 70-cm-thick snowpack, as shown in Fig. 4(a). The simulations show that brightness temperatures increase, particularly that for 36.5 GHz. This "reverse" behavior is because 36.5 GHz can only "see" the top layers when the snow is thick. The new snow

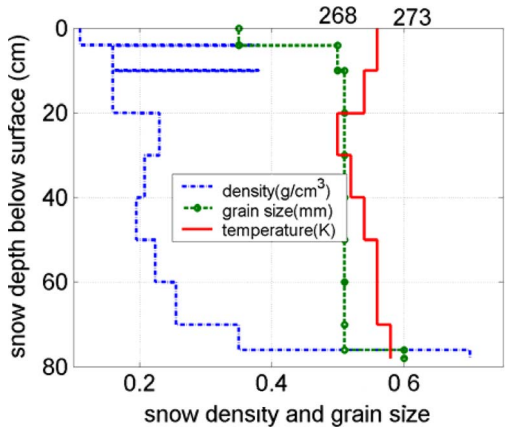

Fig. 6. Snow profile of density, grain size, and temperature on February 21, 2003, at LSOS. The numbers in the bottom of the profile are the values of snow density and grain size, whereas the numbers in the top are the snow temperatures.

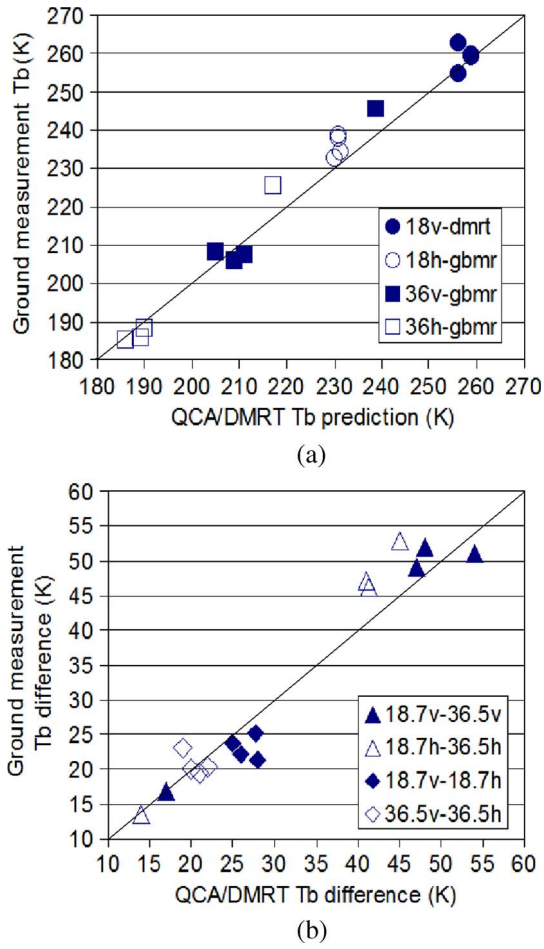

Fig. 7. Multilayer DMRT model Tb simulation and GBMR ground observation, (a) Comparison of Tb's between simulation and GBMR observation. (b) Comparison of polarization difference (18.7v–18.7h and 36.5v–36.5h) and frequency difference (18.7v–36.5v and 18.7h–36.5h).

with smaller grain sizes in the top layer decreases the attenuation effects of 36.5 GHz. The average grain size of the whole snowpack also decreases, so the Tb of 18.7 GHz also increases while not as much as that of 36.5 GHz. This is consistent with Tb observation when snow is thick [14]. In Fig. 5(a), we show another two snow profiles. The dark layer represents a crust

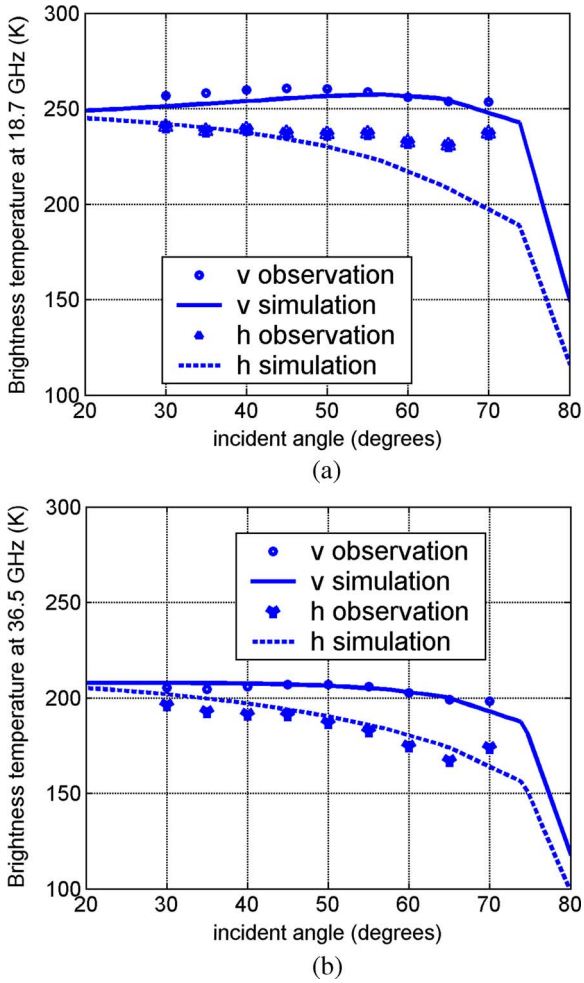

Fig. 8. Multilayer DMRT model Tb simulation and GBMR ground observation at different observation angles on February 20, 2003. (a) 18.7 GHz. (b) 36.5 GHz.

with a density of 0.5 g/cm^3; grain size and temperature are the same as the layer beneath it. The simulated Tb showed that the Tb for 36.5 GHz increases as snow depth increases and can be higher than the Tb for 18.7-GHz horizontal polarizations. In Fig. 5, the ground is smooth; the polarization difference of 18.7 GHz is higher than that of 36.5 GHz because of the reflectivity at the snow–ground interface. Moreover, in the snow profile of Fig. 5(a), the polarization difference of 18.7 GHz is even greater than the frequency difference of vertical polarization, so the Tb for 36.5v is higher than the Tb for 18.7h. The Tb increases after adding the fine-grained new snow. The Tb for 36.5 GHz increases faster than that for 18.7 GHz, and finally, the Tb for 36.5h increases higher than the Tb for 18.7h, too.

IV. Comparison With Ground Measurements

To evaluate the model, we compared the simulated brightness temperatures derived from measured snowpack properties at LSOS of the CLPX experiments in Colorado, USA [21], and the observed brightness temperatures using the GBMR brightness temperature observations of the snow cover at LSOS [22]. LSOS is a 100-m $\times$ 100-m study site which has flat topography with a uniform pine forest, a discontinuous pine forest, and a

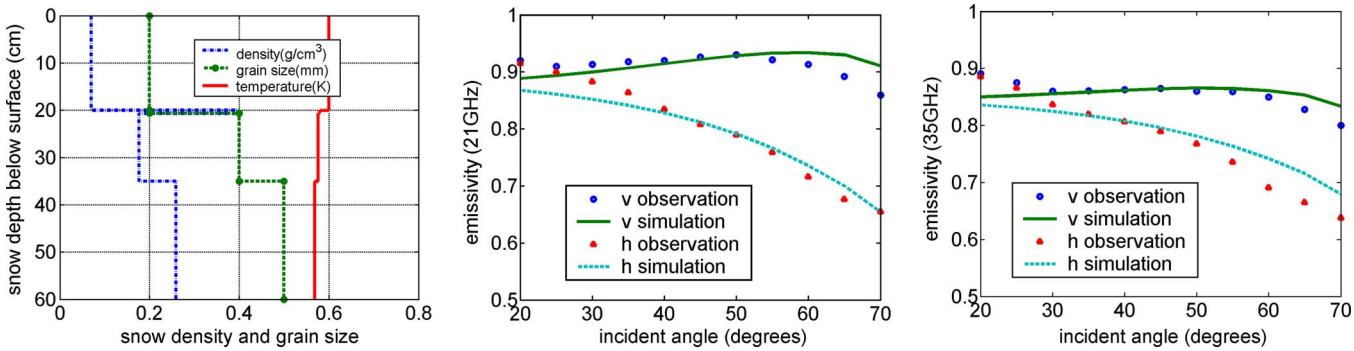

Fig. 9. Multilayer DMRT model emissivity simulation compared with ground observation on December 21, 1995, from [15]. (a) Snow profile of grain size, density, and temperature. The numbers in the bottom of the profile are the values of snow density and grain size, whereas the numbers in the top are the snow temperatures. (b) Comparison of emissivity at 21 GHz. (c) Comparison of emissivity at 35 GHz.

small clearing. We compare the simulated Tb with the measured Tb on December 11, 2002, and February 19, 20, and 21, 2003. The snow parameters shown in Fig. 6 are from snow pit measurements taken on February 21, 2003, at snow pit #2, which was located at about 10 m from the GBMR-7 radiometer view area [21], [22]. The snow pit measurements showed that there are two layers of thin crust near the surface and discontinuous basal crust near the ground. The thin crust is modeled as a 0.6-cm snow layer with a density of 0.38 g/cm^3. The basal crust is modeled as a 2-cm snow layer with a density of 0.38 g/cm^3. The densities of the other layers increase with small fluctuation as the snow depth increases. The grain sizes provide the best fit of the simulations to the observations, which increase as snow depth increases. The grain sizes used here are smaller than the averaged ground measurements. The snow temperature decreases at first and then increases as snow depth increases. We also took the ground temperature to be that of the lowest snow layer. The ground dielectric constant is $3.2 + 0.01i$. We used roughness parameters of $Q = 0.35$ and $H = 1.2$ to improve the match of brightness temperatures with the ground observations. In Fig. 7(a), we show the comparison of brightness temperature between the CLPX data and DMRT model, and in Fig. 7(b), we compare the polarization differences and frequency differences. Brightness temperature, polarization difference, and frequency dependence are in good agreement with the CLPX data. The results of the multilayer model are in much better agreement with the CLPX Tb data than the results of the single-layer model that was presented in [9].

We also compared the model simulations with the GBMR brightness temperature observations at different incident angles from 30° to 70° in Fig. 8. Again, we used the snow profile from the snow pit measurements obtained on February 20, 2003. Because the radiometer was set up on ground, at a fixed height, the footprints vary for different incident angles. The model predictions are about 5 K higher than the field observations at 36.5 GHz at observation angles less than 70°. At a 70° angle, the horizontal polarization is underestimated. The model predictions agree well with observations at 18.7 GHz for vertical and horizontal polarizations at observation angles less than 55°. When observation angles are larger than 55°, the model underestimates the horizontally polarized brightness temperatures.

We also compared the simulated emissivities with the observed emissivities as measured by a portable radiometer at a test site in the Alps, Switzerland [16]. The profiles of density, thickness, and temperature shown in Fig. 9(a) are from [16]. No grain size measurements are available, so we varied the grain size distribution to provide the best fit of the simulations to the observations. The resulting grain size profile was realistic and shown in Fig. 9(a). The ground dielectric constant of $4 + 0.01i$ provides the best fit of the simulations to the observations, with $Q = 0.1$ and $H = 0$. The emissivities from the DMRT model and measurements at 21 and 35 GHz, as a function of observation angles, are in good agreement, as shown in Fig. 9(b) and (c).

V. Conclusion

A multilayer QCA/DMRT model of the microwave emission from a layered snowpack gives more accurate brightness temperatures than a single-layer model, when compared to field observations. The model uses a cubic spline interpolation to connect the intensities at the interfaces. The multilayer QCA/DMRT model simulates the Tb features of various snow profiles and gives greater polarization differences than the single-layer QCA/DMRT model. The simulation results from the multilayer QCA/DMRT model agree well with CLPX ground-based Tb measurements, snow profiles constrained by snow pit measurements, and ground-based emissivity measurements in the Alps. Future applications of the multilayer QCA/DMRT model include merging it with the multilayer hydrology model used by the National Oceanic and Atmospheric Administration (NOAA), NOAA/National Weather Service (NWS) snow model, which is developed at the National Operational Hydrologic Remote Sensing Center of NOAA's NWS [23].

References

[1] L. Tsang, "Passive remote sensing of dense nontenuous media," *J. Electromagn. Waves Appl.*, vol. 1, no. 2, pp. 159–173, 1987.
[2] J. T. Pullianinen, J. Grandell, and M. T. Hallikainen, "HUT snow emission model and its applicability to snow water equivalent retrieval," *IEEE Trans. Geosci. Remote Sens.*, vol. 37, no. 3, pp. 1378–1390, May 1999.
[3] A. Wiesmann and C. Matzler, "Microwave emission model of layered snowpacks," *Remote Sens. Environ.*, vol. 70, no. 3, pp. 307–316, 1999.
[4] L. Tsang, J. A. Kong, and R. Shin, *Theory of Microwave Remote Sensing*. New York: Wiley, 1985.
[5] C. Matzler and A. Wiesmann, "Extension of the microwave emission model of layered snowpacks to coarse-grained snow," *Remote Sens. Environ.*, vol. 70, no. 3, pp. 317–325, Dec. 1999.

[6] L. Tsang, C. T. Chen, A. T. C. Chang, J. Guo, and K. H. Ding, "Dense media radiative transfer theory based on quasicrystalline approximation with application to passive microwave remote sensing of snow," *Radio Sci.*, vol. 35, no. 3, pp. 731–749, May/Jun. 2000.
[7] L. Tsang, J. Pan, D. Liang, Z. X. Li, D. Cline, and Y. H. Tan, "Modeling active microwave remote sensing of snow using dense media radiative transfer (DMRT) theory with multiple scattering effects," *IEEE Trans. Geosci. Remote Sens.*, vol. 45, no. 4, pp. 990–1004, Apr. 2007.
[8] A. T. C. Chang, J. L. Foster, and D. K. Hall, "Nimbus-7 derived global snow cover parameters," *Ann. Glaciol.*, vol. 9, pp. 39–44, 1987.
[9] K. M. Andreadis, D. Liang, L. Tsang, D. P. Lettenmaier, and E. G. Josberger, "Characterization of errors in a coupled snow hydrology microwave emission model," *J. Hydrometeorol.*, vol. 9, no. 1, p. 149, 2007.
[10] M. Tedesco and E. J. Kim, "Retrieval of dry-snow parameters from microwave radiometric data using a dense-medium model and genetic algorithms," *IEEE Trans. Geosci. Remote Sens.*, vol. 44, no. 8, pp. 2143–2151, Aug. 2006.
[11] D. M. Gray and D. H. Male, *Handbook of Snow: Principles, Processes, Management & Use*. Toronto, ON, Canada: Pergamon Press, 1981, pp. 277–278.
[12] E. G. Josberger, P. Gloersen, A. Chang, and A. Rango, "The effects of snowpack grain size on satellite passive microwave observations from the Upper Colorado River Basin," *J. Geophys. Res.*, vol. 101, no. C3, pp. 6679–6688, 1996.
[13] M. Sturm and J. Holmgren, "A seasonal snow cover classification system for local to global applications," *J. Climate*, vol. 8, no. 5, pp. 1261–1283, May 1995.
[14] S. Rosenfeld and N. Grody, "Anomalous microwave spectra of snow cover observed from special sensor microwave/imager measurements," *J. Geophys. Res.*, vol. 105, no. D11, pp. 14 913–14 925, Jun. 2000.
[15] M. Tedesco, E. J. Kim, A. W. England, R. D. De Roo, and J. P. Hardy, "Brightness temperatures of snow melting/refreezing cycles: Observations and modeling using a multilayer dense medium theory-based model," *IEEE Trans. Geosci. Remote Sens.*, vol. 44, no. 12, pp. 3563–3572, Dec. 2006.
[16] A. Wiesmann, T. Strozzi, and T. Weise, "Passive microwave signature catalogue of snowcovers at 11, 21, 35, 48 and 94 GHz," Univ. of Bern, Bern, Switzerland, IAP Research Report 96-8, 1996.
[17] J. R. Wang, P. E. O'Neill, T. J. Jackson, and E. T. Engman, "Multifrequency measurements of the effects of soil moisture, soil texture, and surface roughness," *IEEE Trans. Geosci. Remote Sens.*, vol. GRS-21, no. 1, pp. 4–51, Jan. 1983.
[18] C. D. Boor, *A Practical Guide to Splines*. New York: Springer-Verlag, 1978, pp. 49–57.
[19] L. Tsang, J. A. Kong, K. H. Ding, and C. O. Ao, "Scattering of Electromagnetic Waves," in *Numerical Simulations*, vol. 2. New York: Wiley-Interscience, 2001, pp. 424–425.
[20] M. T. Hallikainen, F. T. Ulaby, and T. E. Deventer, "Extinction behavior of dry snow in the 18 to 90 GHz range," *IEEE Trans. Geosci. Remote Sens.*, vol. GRS-25, no. 6, pp. 737–745, Nov. 1987.
[21] J. Hardy, J. Pomeroy, T. Link, D. Marks, D. Cline, K. Elder, and R. Davis, *CLPX-Ground: Snow Measurements at the Local Scale Observation Site (LSOS)*. Boulder, CO: Nat. Snow and Ice Data Center, Digital Media, 2003.
[22] T. Graf, T. Koike, H. Fujii, M. Brodzik, and R. Armstrong, *CLPX-Ground: Ground Based Passive Microwave Radiometer (GBMR-7) Data*. Boulder, CO: National Snow and Ice Data Center, Digital Media, 2003.
[23] L. Li, D. Cline, G. Fall, A. Rost, and A. Nilsson, "Performance and suitability of single- and multiple-layer snow models for operational, moderate-resolution, CONUS snow data assimilation," in *Proc. 58th Eastern Snow Conf.*, Ottawa, ON, Canada, 2001.

Ding Liang (S'07) received the B.Eng. degree in electrical engineering from Wuhan University, Wuhan, China. She is currently working toward the Ph.D. degree in the Department of Electrical Engineering, University of Washington, Seattle.

Her current research interests include theoretical and numerical studies of electromagnetic wave propagation and scattering in random media and remote sensing.

Xiaolan Xu received the B.Eng. degree in electrical engineering from Zhejiang University, Hangzhou, China. She is working toward the Ph.D. degree in the Department of Electrical Engineering, University of Washington, Seattle.

She is now a Research Assistant in Laboratory of Applications and Computations in Electromagnetics and Optics, Department of Electrical Engineering, University of Washington. Her research interests include theoretical and numerical studies of electromagnetic wave propagation, scattering in random media and snow remote sensing.

Leung Tsang (S'73–M'75–SM'85–F'90) received the B.S., M.S., and Ph.D. degrees from the Massachusetts Institute of Technology, Cambridge.

He is currently a Professor and the Associate Chairman for Education with the Department of Electrical Engineering, University of Washington, Seattle, where he has been teaching since 1983. Between 2001 and 2004, while on leave, he was the Chair Professor and the Assistant Head with the Department of Electronic Engineering, City University of Hong Kong, Kowloon. He is the author of four books, namely, *Theory of Microwave Remote Sensing*; *Scattering of Electromagnetic Waves, Vol. 1: Theory and Applications*; *Scattering of Electromagnetic Waves, Vol. 2: Numerical Simulations*; and *Scattering of Electromagnetic Waves, Vol. 3: Advanced Topics*. His current research interests include remote sensing and geoscience applications, multiple scattering of waves, signal integrity, computational electromagnetics, and wireless communications.

Dr. Tsang is a Fellow of the Optical Society of America. He has been the President of the IEEE Geoscience and Remote Sensing Society (GRSS) since January 2006. He was the Editor-in-Chief of the IEEE TRANSACTIONS ON GEOSCIENCE AND REMOTE SENSING from 1996 to 2001. He was the General Chairman of the 1998 IEEE International Geoscience and Remote Sensing Symposium. He received the IEEE GRSS Outstanding Service Award in 2000. He was also the recipient of the IEEE Third Millennium Medal in 2000.

Konstantinos M. Andreadis received the Engineering Diploma in environmental engineering from the Technical University of Crete, Chania, Greece, and the M.Sc.E. degree in civil and environmental engineering from the University of Washington, Seattle, where he is currently working toward the Ph.D. degree in the Department of Civil and Environmental Engineering.

Edward G. Josberger received the B.S. degree from the New York University, New York, NY, and the Ph.D. degree from the University of Washington, Seattle.

He is currently a Senior Scientist and the Chief of the Ice and Climate Project with the U.S. Geological Survey, Washington Water Science Center, Tacoma, WA. His research interests include understanding the response of glaciers in the Pacific Northwest and Alaska to fluctuations in atmospheric circulation. This includes assessing the impact of glacial retreat on the hydrology of glacierized basins. He has a particular interest in the circulation of fjords with tide water glaciers and lakes that are dammed or bounded by glaciers and the resulting ecosystems. In his studies, he also carries out remote sensing research to develop and apply new techniques to observe glaciers and snowpacks using optical, as well as passive and active microwave, sensors. He collaborates with the University of Michigan, Ann Arbor; Michigan Technical Research Institute, Ann Arbor; the University of Washington, Seattle; NASA, Washington, D.C.; the Centre d'Etudes Spatiales de la BIOsphere (CESBIO), Toulouse, France; and the French Space Agency, Paris, France.